Transition Finite Element Families for Adaptive Analysis of Axisymmetric Elasticity Problems

K.Y.Sze*, **D.Wu**[1]

Departments of Mechanical Engineering, The University of Hong Kong, Pokfulam, Hong Kong SAR, P.R.China.

*Correspondence author (email: kysze@hku.hk)

1 Present address: *Altair Engineering Software (Shanghai), Yangshupu Road, Shanghai 200082, P.R.China.*

ABSTRACT

In this paper, four transition element families which comprise five- to seven-node quadrilateral elements are developed based on the hybrid-stress and enhanced assumed strain (EAS) formulations for adaptive analyses of axisymmetric elasticity problems. For members in the first hybrid-stress family, a stress field with ten equilibrating stress modes is derived and employed by all members of the family. To study the effect of including more stress modes, another family with two additional stress modes is implemented. On the other hand, two EAS element families are constructed with respect to the incompatible displacement modes of two existing incompatible displacement transition element families. Several numerical examples are exercised. It can be seen that the first hybrid-stress family is the most accurate one among the proposed families. Moreover, the EAS families are close to the respective incompatible families in accuracy yet the former families are not only more efficient in computation but also more concise in formulation.

Keywords: hybrid-stress, EAS, axisymmetric, adaptive analysis, transition element

Published in *Finite Elements in Analysis & Design* 47 (2011) 360-372
doi:10.1016/j.finel.2010.11.002

1. INTRODUCTION

In adaptive analysis, the finite element mesh is locally refined according to estimated error through repeating the working cycle comprising finite element analysis, stress recovery, error estimation and mesh refinement until the estimated error is brought below a prescribed value. The basic adaptive refinement techniques can be categorized into *h*-refinement, *p*-refinement and *r*-refinement. For *p*- and *r*-refinement, interested readers may refer to reference [1] for a review. In *h*-refinement, an element whose error is larger than the prescribed value is subdivided into smaller elements. The subdivision creates transition elements in which some of their edges possess mid-side nodes, see Figure 1. Along these edges, the displacement must be piecewise linear in order to be compatible with the displacement in the subdivided elements. In this paper, *ad hoc* transition element families will be developed by hybrid-stress and enhanced assumed strain (EAS) methods for axisymmetric elasticity problems.

In recent decades, various advanced four-node axisymmetric elements have been developed. These include incompatible elements, enhanced assumed strain elements and hybrid-stress elements [2-11]. On the other hand, transition elements for *h*-refinement adaptive analysis are relative rare. It appears that the only advanced transition element family for axisymmetric analyses is the NQV family [12]. In NQV, different incompatible modes were developed for elements with different combinations of mid-side nodes. To pass the patch test, the incompatible B-matrix relating the element strains and incompatible displacement modes is modified by a B-bar method in which the incompatible B-matrix is shifted by its own pre-computed domain average.

For plane elasticity problems, the authors have recently developed three families of quadrilateral transition elements [13-14]. The first family is based on the hybrid-stress formulation and was developed by adopting a complete linear equilibrating stress field which is employed by all members in the family. The second and third element families were developed by devising EAS fields [5] based on the incompatible transition element families of Choi et al [12, 15]. Similar works have also undertaken for 3D elasticity problems [13-14].

The present paper can be considered as an extension of our previous effort on 2D and 3D elasticity analysis. New hybrid-stress and EAS transition element families are derived for axisymmetric elasticity problems. For the hybrid-stress element, it is first noted the equilibrium

conditions can be expressed as linear differential equations with constant coefficients in terms of ($r\sigma_r$, σ_θ, $r\sigma_z$, $r\tau_{rz}$). For the first hybrid-stress element family, the field for ($r\sigma_r$, σ_θ, $r\sigma_z$, $r\tau_{rz}$) is equilibrating and complete linear in (r, z) with ten modes. Instead of devising different sets of stress modes for elements with different combinations of mid-side nodes, the idea proposed by Wan and his co-workers [16-17] who employ the same set of stress modes for all transition elements is adopted. To study the effect of additional stress modes, another family with two additional stress modes is implemented. On the other hand, two EAS transition element families are developed based on the incompatible displacement modes of the axisymmetric and 3D transition element families of Choi et al [12, 15]. Unlike the incompatible B-matrices in the element families of Choi et al, the domain integral of the EAS modes vanish identically and the B-bar method that computationally modifies the incompatible B-matrices can be exempted. Both EAS families pass the patch test and retain the accuracy of the incompatible families. Lastly, several examples are examined. The errors or estimated errors of various transition element families are compared.

2. REVIEW OF STANDARD ISOPARAMETRIC DISPLACEMENT ELEMENT

A transition element can possess 1, 2 or 3 mid-side nodes in addition to the four corner nodes as depicted in Figure 2. For the sake of assuring the compatibility, Gupta [18] introduced the piecewise linear displacement interpolation functions for the transition element which is compatible with its adjacent regular four-node quadrilateral elements. All transition elements which to be considered in this paper will adopt Gupta's displacement interpolation functions. It should be remarked that the derivatives of the functions are discontinuous within the element. If derivatives appear in an integral, it is necessary to divide the integration domain into sub-domains as shown in Figure 2 along the lines of discontinuity.

2.1 Gupta's Shape Functions for 2D Transition Elements

Consider the quadrilateral transition element with at most three mid-side nodes as shown in Figure 2. Gupta's shape functions of the mid-side nodes in terms of the element's natural coordinates ξ and $\eta \in$ [-1, +1] can be expressed as:

$$N_5 = \frac{\Delta_5}{2}(1-|\xi|)(1-\eta),\ N_6 = \frac{\Delta_6}{2}(1+\xi)(1-|\eta|),\ \ N_7 = \frac{\Delta_7}{2}(1-|\xi|)(1+\eta),\ \ N_8 = \frac{\Delta_8}{2}(1-\xi)(1-|\eta|)$$

(1)

where | | returns the magnitude of embraced term and

$$\Delta_i = \begin{cases} 1 & \text{if the } i\text{-th node exists} \\ 0 & \text{otherwise} \end{cases}.$$

Owing to the magnitude operator, derivatives of these shape functions in (1) are discontinuous at $\xi = 0$ and/or $\eta = 0$. The interpolation functions for the corner nodes are

$$N_1 = \frac{1}{4}(1-\xi)(1-\eta) - \frac{1}{2}(N_5 + N_8),\ \ N_2 = \frac{1}{4}(1+\xi)(1-\eta) - \frac{1}{2}(N_5 + N_6),$$

$$N_3 = \frac{1}{4}(1+\xi)(1+\eta) - \frac{1}{2}(N_6 + N_7),\ \ N_4 = \frac{1}{4}(1-\xi)(1+\eta) - \frac{1}{2}(N_7 + N_8) \qquad (2)$$

2.2 Element Stiffness Matrix

With the aforementioned functions, the displacement for an m-node transition element can be interpolated as:

$$\mathbf{u} = \begin{Bmatrix} u_r \\ u_z \end{Bmatrix} = [\, N_1\mathbf{I}_{2\times2} \quad N_2\mathbf{I}_{2\times2} \quad \cdots \quad N_m\mathbf{I}_{2\times2} \,] \begin{Bmatrix} \mathbf{u}_1 \\ \vdots \\ \mathbf{u}_m \end{Bmatrix} = \mathbf{Nq} \qquad (3)$$

in which the displacement vector **u**, interpolation matrix **N** and element displacement vector **q** are self-defined whereas *r* and *z* denotes radial and longitudinal coordinates, respectively. The vectors of strain **ε** and stress **σ** can be derived to be:

$$\boldsymbol{\varepsilon} = \begin{Bmatrix} \varepsilon_r \\ \varepsilon_z \\ \gamma_{rz} \\ \varepsilon_\theta \end{Bmatrix} = \begin{bmatrix} \partial/\partial r & 0 \\ 0 & \partial/\partial z \\ \partial/\partial z & \partial/\partial r \\ 1/r & 0 \end{bmatrix} \begin{Bmatrix} u_r \\ u_z \end{Bmatrix} = \boldsymbol{D}(\mathbf{Nq}) = \mathbf{B}_c\mathbf{q} \quad , \quad \boldsymbol{\sigma} = \begin{Bmatrix} \sigma_r \\ \sigma_z \\ \sigma_{rz} \\ \sigma_\theta \end{Bmatrix} = \mathbf{C}\boldsymbol{\varepsilon} \qquad (4)$$

where the strain-displacement operator matrix ***D*** and the strain-displacement matrix $\mathbf{B}_c$ are self-defined. On the other hand, θ denotes the circumferential direction and **C** is the elasticity matrix. As $\mathbf{B}_c$ gives the strain from the compatible interpolated displacement, it will be termed as the compatible B-matrix.

The total potential of an element can be expressed as:

$$\prod_p^e = \frac{1}{2}\int_{\Omega^e} \boldsymbol{\varepsilon}^T \mathbf{C}\boldsymbol{\varepsilon} d\Omega^e - W^e \tag{5}$$

where Ω^e denotes the volume of an axisymmetric element and W^e is the elemental work potential. Introduce (4) into (5), we obtain

$$\prod_p^e = \frac{1}{2}\mathbf{q}^T \left(\int_{\Omega^e} \mathbf{B}_c{}^T \mathbf{C}\mathbf{B}_c d\Omega\right)\mathbf{q} - W^e \quad \text{and} \quad \int_{\Omega^e} \circ\, d\Omega = 2\pi \int_{-1}^{+1}\int_{-1}^{+1} \circ\, r \det(\mathbf{J}) d\xi d\eta \tag{6}$$

where the braced term in the first expression is the element stiffness matrix and

$$\mathbf{J} = \begin{bmatrix} \partial r / \partial \xi & \partial z / \partial \xi \\ \partial r / \partial \eta & \partial z / \partial \eta \end{bmatrix} \tag{7}$$

is the Jacobi matrix. As $\mathbf{B}_c$ is discontinuous across along $\xi = 0$ and/or $\eta = 0$, the integration domain $\xi \times \eta \in [-1,+1]\times[-1,+1]$ has to be split into small domains along the lines of discontinuity, see Figure 2.

3. HYBRID-STRESS TRANSITION ELEMENT

Displacement compatible elements are always too stiff. Hybrid-stress elements with an independent assumed stress field may provide more accurate predictions [3, 6-7, 9]. In this section, a new family of axisymmetric hybrid-stress transition elements will be developed by using Hellinger-Reissner principle in this section.

3.1 Element Stiffness Formulation via the Hellinger-Reissner Variational Principle

The elemental Hellinger-Reissner functional can be written as:

$$\prod_{HR}^e = \int_{\Omega^e} [-\frac{1}{2}\boldsymbol{\sigma}^T \mathbf{C}^{-1}\boldsymbol{\sigma} + \boldsymbol{\sigma}^T (\boldsymbol{D}\mathbf{u})] d\Omega - W^e \tag{8}$$

where $\boldsymbol{\sigma}$ is an independent assumed stress. All other terms have been defined in (3) and(4). The assumed stress can be expressed as:

$$\boldsymbol{\sigma} = \mathbf{P}\boldsymbol{\beta} \tag{9}$$

in which **P** is the stress shape function matrix and $\boldsymbol{\beta}$ is the vector of coefficients. With the compatible displacement (3), substitution of (9) into (8) gives

$$\prod_{HR}^{e} = -\frac{1}{2}\boldsymbol{\beta}^T\mathbf{H}\boldsymbol{\beta} + \boldsymbol{\beta}^T\mathbf{G}\mathbf{q} - W^e \tag{10}$$

in which

$$\mathbf{H} = \int_{\Omega^e} \mathbf{P}^T\mathbf{C}^{-1}\mathbf{P}d\Omega \quad , \quad \mathbf{G} = \int_{\Omega^e} \mathbf{P}^T(\boldsymbol{D}\mathbf{N})d\Omega\,. \tag{11}$$

As the assumed stress of an element is independent of the others, the stationary condition of $\prod_{HR}^{e}$ with respect to $\boldsymbol{\beta}$ leads to

$$\boldsymbol{\beta} = \mathbf{H}^{-1}\mathbf{G}\mathbf{q} \tag{12}$$

Back substitution of (12) into (10) results in

$$\prod_{HR}^{e} = \frac{1}{2}\mathbf{q}^T(\mathbf{G}^T\mathbf{H}^{-1}\mathbf{G})\mathbf{q} - W^e \tag{13}$$

in which the embraced term is the element stiffness matrix of the hybrid-stress element.

3.2 Same Set of Stress Modes for All Transition Elements

To design a hybrid-stress element, one should consider the number of stress modes in the stress field, or simply dim.($\boldsymbol{\beta}$). For a rank-sufficient element, the following condition must be satisfied:

$$\text{dim.}(\boldsymbol{\beta}) \geq \text{dim.}(\mathbf{q}) - \text{number of rigid body modes.} \tag{14}$$

On the other hand, when dim.($\boldsymbol{\beta}$) is excessive, the element will be excessively stiff. Indeed, many successful hybrid-stress elements adopt dim.($\boldsymbol{\beta}$) = dim.($\mathbf{q}$) – number of rigid body modes [19-20]. In axisymmetric problems, there is only one rigid body mode which is the translation along the *z* direction.

With respect to (14), the 5-, 6- and 7-node transition elements require at least 9, 11 and 13 stress modes for rank-sufficiency, respectively. While it is possible to devise stress field with the corresponding numbers of stress modes, a single stress field with a fixed number of stress modes will be employed for several reasons. Firstly, it is more convenient to use a single set of stress modes for computer implementation. Secondly, rank deficient-elements are more efficient than rank

sufficient elements. Thirdly, all transition elements are connected with rank-sufficient four-node elements, the spurious zero energy modes of the transition elements would be suppressed by its neighbourhoods and the global stiffness matrix is always rank-sufficient. Lastly, rank sufficient elements do not necessary lead to higher accuracy as revealed in the previous work on 2D/3D hybrid-stress transition elements [13-14]. In this light, the idea of using the same set of stress modes for all transition elements will be adopted here.

3.3 Hybrid-stress Transition Elements with Ten Stress Modes

In developing axisymmetric hybrid-stress elements, the stress modes can be designed in the natural coordinate system and the physical stress modes can be obtained by coordinate transformation [9, 21]. Alternatively, the stress modes can be designed directly in the physical cylindrical coordinate system [6, 22]. The latter approach will be employed for the obvious advantage that the stress modes can satisfy the stress equilibrium condition. The condition is commonly expressed as:

$$\frac{\partial \sigma_r}{\partial r} + \frac{\partial \tau_{rz}}{\partial z} + \frac{\sigma_r - \sigma_\theta}{r} = 0 \quad , \quad \frac{\partial \tau_{rz}}{\partial r} + \frac{\partial \sigma_z}{\partial z} + \frac{\tau_{rz}}{r} = 0 \tag{15}$$

which are linear differential equation with non-constant coefficient $1/r$.

In transition hybrid-stress elements for 2D/3D problems [13-14], it is noted that complete linear and equilibrating stress fields deliver the best accuracy. If one starts with 1, r and z terms for (σ_r, σ_θ, σ_z, τ_{rz}) in (15), $1/r$ terms must be included for fulfilling the equilibrium condition. However, when (15) is expressed in terms of ($r\sigma_r$, σ_θ, $r\sigma_z$, $r\tau_{rz}$), the condition becomes

$$\frac{\partial (r\sigma_r)}{\partial r} + \frac{\partial (r\tau_{rz})}{\partial z} - \sigma_\theta = 0 \quad , \quad \frac{\partial (r\sigma_z)}{\partial z} + \frac{\partial (r\tau_{rz})}{\partial r} = 0 \tag{16}$$

which posses only constant coefficients. We start with 1, r and $z' = z - z_0$ uncoupled modes for each of $r\sigma_r$, σ_θ, $r\sigma_z$ and $r\tau_{rz}$ where z_0 equals $(z_1 + z_2 + z_3 + z_4)/4$, i.e., the average of z-coordinate of the four element corner nodes. The practice avoids the potential numerical error induced by large z-value. By imposing the equilibrium condition on the twelve uncoupled modes, the following ten-modes equilibrating field can be devised:

$$\begin{Bmatrix} r\sigma_r \\ r\sigma_z \\ r\tau_{rz} \\ \sigma_\theta \end{Bmatrix} = \begin{bmatrix} 1 & r & z' & 0 & 0 & 0 & 0 & 0 & r^2/2 & rz' \\ 0 & 0 & 0 & 1 & r & z' & 0 & 0 & 0 & 0 \\ 0 & 0 & 0 & 0 & 0 & -r & z' & 1 & 0 & 0 \\ 0 & 1 & 0 & 0 & 0 & 0 & 1 & 0 & r & z' \end{bmatrix} \begin{Bmatrix} \beta_1 \\ \vdots \\ \vdots \\ \beta_{10} \end{Bmatrix} \tag{17}$$

or, equivalently,

$$\boldsymbol{\sigma} = \begin{Bmatrix} \sigma_r \\ \sigma_z \\ \tau_{rz} \\ \sigma_\theta \end{Bmatrix} = \mathbf{P}\boldsymbol{\beta} = \begin{bmatrix} 1/r & 1 & z'/r & 0 & 0 & 0 & 0 & 0 & r/2 & z' \\ 0 & 0 & 0 & 1/r & 1 & z'/r & 0 & 0 & 0 & 0 \\ 0 & 0 & 0 & 0 & 0 & -1 & z'/r & 1/r & 0 & 0 \\ 0 & 1 & 0 & 0 & 0 & 0 & 1 & 0 & r & z' \end{bmatrix} \begin{Bmatrix} \beta_1 \\ \vdots \\ \vdots \\ \beta_{10} \end{Bmatrix}. \tag{18}$$

In particular, the $r^2/2$ and rz' terms in $r\sigma_r$ are employed to balance the r and z' terms in σ_θ. The former terms can also be balanced by additional terms in $r\tau_{rz}$ which, however, would adversely affect the accuracy of the elements in bending-dominated circular plate and cylinder problems.

It can be seen that some components in (18) possess the $1/r$ singularity but so do the circumferential strain derived from the interpolated displacement and other hybrid-stress finite element models [6, 22]. In practice, the singularity issue does not bother as element matrices are evaluated by numerical integrations and stress is constructed by using the value at the Gaussian points which are away from $r = 0$. The transition element family based on the above 10β field is denoted as AHS-10 and the 2×2 Gauss numerical integral will be employed to calculate the H-matrix. Due to the discontinuity of derivatives of the N-matrix, the integration area for calculating G-matrix is split into parts according to the existence of the mid-side nodes, see Figure 2.

Returning to the issue on the number of stress modes, the stress field in (18) is only sufficient to secure the full rankness of the five-node transition elements. Hence, it is not rational to further reduce the number. To illustrate that the number of modes is practically optimal, the following two modes are augmented to (18):

$$\begin{bmatrix} 0 & rz'/2 \\ z' & 0 \\ -r/2 & 0 \\ 0 & rz' \end{bmatrix} \begin{Bmatrix} \beta_{11} \\ \beta_{12} \end{Bmatrix}. \tag{19}$$

to form a twelve-mode field. The number of stress modes is considerably above the optimized number indicated in (14) and leads to overly stiff five-node transition elements which are the

dominating elements in number among the transition elements. The section on numerical study also reveals that the ten-mode stress field yields more accurate predictions than the twelve-mode field does.

4. REVIEW OF INCOMPATIBLE MODES

In this study, two EAS transition element families will be developed based on Choi's incompatible modes of Choi et al[12, 15]. Here, the incompatible modes are briefly reviewed. In incompatible elements [22], the interpolated and compatible displacement $\mathbf{u}_c$ is enriched by an incompatible displacement $\mathbf{u}_\lambda$. The displacement and strain become:

$$\mathbf{u} = \mathbf{u}_c + \mathbf{u}_\lambda = \mathbf{N}\mathbf{q} + \mathbf{M}\boldsymbol{\lambda} \quad , \quad \boldsymbol{\varepsilon} = \boldsymbol{D}\mathbf{u} = \boldsymbol{D}\mathbf{u}_c + \boldsymbol{D}\mathbf{u}_\lambda = (\boldsymbol{D}\mathbf{N})\mathbf{q} + (\boldsymbol{D}\mathbf{M})\boldsymbol{\lambda} = \mathbf{B}_c\mathbf{q} + \mathbf{B}_\lambda\boldsymbol{\lambda} \tag{20}$$

where $\mathbf{M}$ is the incompatible displacement shape function matrix and $\boldsymbol{\lambda}$ is the vector of coefficients. $\mathbf{B}_c$ and $\mathbf{B}_\lambda$ are self-defined. The requirement for an incompatible element to pass the patch test is

$$\int_{\Omega^e} \mathbf{B}_\lambda d\Omega = 0 \tag{21}$$

To enable the incompatible element to pass the patch test, approximate strain-displacement operators had been used [23]. On the other hand, Choi et al [12] presented two families of incompatible modes for transition elements. With the B-bar method, the strain is modified as:

$$\boldsymbol{\varepsilon} = \mathbf{B}_c\mathbf{q} + \mathbf{B}_\lambda^*\boldsymbol{\lambda} \tag{22}$$

in which

$$\mathbf{B}_\lambda^* = \mathbf{B}_\lambda - \frac{1}{\Omega^e}\int_{\Omega^e} \mathbf{B}_\lambda d\Omega \quad \text{and} \quad \int_{\Omega^e} \mathbf{B}_\lambda^* d\Omega = 0\,. \tag{23}$$

4.1 Nonconforming Axisymmetric Quadrilateral Variable-Node (NQV) Elements

The incompatible displacement shape functions given by Choi et al for the NQV axisymmetric transition element family in [12] can be expressed as:

$$\text{5- and 6-node elements: } \begin{cases} M_\xi = (1-\xi^2)[1 - \dfrac{\Delta_5}{2}(1-\eta) - \dfrac{\Delta_7}{2}(1+\eta)] \\ M_\eta = (1-\eta^2)[1 - \dfrac{\Delta_6}{2}(1+\xi) - \dfrac{\Delta_8}{2}(1-\xi)] \end{cases}, \tag{24}$$

$$\text{7-node elements: } M_b = (1-\xi^2)(1-\eta^2)\,. \tag{25}$$

For a transition element with m (= 1, 2) non-zero incompatible displacement shape functions, the incompatible displacement is:

$$\mathbf{u}_\lambda = \mathbf{M}\boldsymbol{\lambda} = \left[\, M_1\mathbf{I}_{2\times 2} \quad \cdots \quad M_m\mathbf{I}_{2\times 2} \,\right]\boldsymbol{\lambda}\,. \tag{26}$$

4.2 Nonconforming Variable-Node (NCV) Elements

Choi and Lee [15] also presented another family of incompatible transition elements for 3D elastic problems whose incompatible modes are different from those of NQV. These 3D incompatible modes can be degenerated as

$$M_1 = (1-\xi^2) - (N_5 + N_7) \quad , \quad M_2 = (1-\eta^2) - (N_6 + N_8) \tag{27}$$

for plane and axisymmetric elements.

5. ENHANCED ASSUMED STRAIN TRANSITION ELEMENTS

Although an incompatible element satisfying (21) can be obtained by B-bar method as described in (22) and (23). However, it is computationally more efficient if $\mathbf{B}_\lambda$***** is explicit. In this section, the task will be attained by using enhanced assumed strain method (EAS) [5]. The core idea of EAS method is that the compatible strain field $\boldsymbol{\varepsilon}_c$ is enhanced by an assumed strain field $\boldsymbol{\varepsilon}_\lambda$ as

$$\boldsymbol{\varepsilon} = \boldsymbol{\varepsilon}_c + \boldsymbol{\varepsilon}_\lambda = \mathbf{B}_c\mathbf{q} + \mathbf{E}\boldsymbol{\lambda} \tag{28}$$

where $\mathbf{E}$ is the EAS shape function matrix and $\boldsymbol{\lambda}$ is the vector of coefficients. Similar to incompatible elements, the requirement for the element to pass the patch test is

$$\int_{\Omega^e} \mathbf{E}\,d\Omega = \mathbf{0} \qquad \text{or} \qquad \int_{\Omega^e} \boldsymbol{\varepsilon}_\lambda\,d\Omega = \mathbf{0}\,. \tag{29}$$

The difference between the EAS and the incompatible displacement method is that the EAS modes need not to be derived from the incompatible displacement modes through either the exact or an approximate strain-displacement operator.

5.1 EAS Formulation for Axisymmetric Problems

In this paper, however, the incompatible modes of Choi et al will be employed to derive the EAS modes. To this end, the M-matrices discussed in the last section are used as the shape function matrix of the covariant displacement $\{u_\xi, u_\eta\}^T$ which is related to the physical displacement as:

$$\begin{Bmatrix} u_r \\ u_z \end{Bmatrix} = \mathbf{J}^{-1}\begin{Bmatrix} u_\xi \\ u_\eta \end{Bmatrix} = \mathbf{J}^{-1}\begin{Bmatrix} u_\xi \\ u_\eta \end{Bmatrix} = \begin{bmatrix} \xi_r & \eta_r \\ \xi_z & \eta_z \end{bmatrix}\begin{Bmatrix} u_\xi \\ u_\eta \end{Bmatrix} = \begin{bmatrix} \xi_r & \eta_r \\ \xi_z & \eta_z \end{bmatrix}\mathbf{M}\boldsymbol{\lambda} \tag{30}$$

in which

$$\mathbf{J} = \begin{bmatrix} \partial r/\partial\xi & \partial z/\partial\xi \\ \partial r/\partial\eta & \partial z/\partial\eta \end{bmatrix} \quad \text{and} \quad \mathbf{J}^{-1} = \begin{bmatrix} \xi_r & \eta_r \\ \xi_z & \eta_z \end{bmatrix} = \begin{bmatrix} \partial\xi/\partial r & \partial\eta/\partial r \\ \partial\xi/\partial z & \partial\eta/\partial z \end{bmatrix}. \tag{31}$$

With the strain-displacement relation in (4) and the chain rule, the physical EAS field is:

$$\boldsymbol{\varepsilon}_\lambda = \begin{Bmatrix} \varepsilon_r \\ \varepsilon_z \\ \gamma_{rz} \\ \varepsilon_\theta \end{Bmatrix}_\lambda = \boldsymbol{D}\begin{Bmatrix} u_r \\ u_z \end{Bmatrix}_\lambda = \left(\begin{bmatrix} \xi_r(\partial/\partial\xi) + \eta_r(\partial/\partial\eta) & 0 \\ 0 & \xi_z(\partial/\partial\xi) + \eta_z(\partial/\partial\eta) \\ \xi_z(\partial/\partial\xi) + \eta_z(\partial/\partial\eta) & \xi_r(\partial/\partial\xi) + \eta_r(\partial/\partial\eta) \\ 1/r & 0 \end{bmatrix} \begin{bmatrix} \xi_r & \eta_r \\ \xi_z & \eta_z \end{bmatrix} \right) \mathbf{M}\boldsymbol{\lambda} \tag{32}$$

With all terms but the differential operators $\partial/\partial\xi$ and $\partial/\partial\eta$ within the round brackets to be replaced by their counterparts at $\xi = \eta = 0$, the following approximation can be obtained:

$$\boldsymbol{\varepsilon}_\lambda \simeq \begin{bmatrix} \bar{\xi}_r\bar{\xi}_r & \bar{\eta}_r\bar{\eta}_r & \bar{\xi}_r\bar{\eta}_r & 0 \\ \bar{\xi}_z\bar{\xi}_z & \bar{\eta}_z\bar{\eta}_z & \bar{\xi}_z\bar{\eta}_z & 0 \\ 2\bar{\xi}_r\bar{\xi}_z & 2\bar{\eta}_r\bar{\eta}_z & \bar{\xi}_r\bar{\eta}_z + \bar{\xi}_z\bar{\eta}_r & 0 \\ 0 & 0 & 0 & 1 \end{bmatrix} \begin{bmatrix} \partial/\partial\xi & 0 \\ 0 & \partial/\partial\eta \\ \partial/\partial\eta & \partial/\partial\xi \\ \bar{\xi}_r/\bar{r} & \bar{\eta}_r/\bar{r} \end{bmatrix} \mathbf{M}\boldsymbol{\lambda} = \mathbf{T} \begin{bmatrix} \partial/\partial\xi & 0 \\ 0 & \partial/\partial\eta \\ \partial/\partial\eta & \partial/\partial\xi \\ \bar{\xi}_r/\bar{r} & \bar{\eta}_r/\bar{r} \end{bmatrix} \mathbf{M}\boldsymbol{\lambda} \tag{33}$$

where

$$\begin{bmatrix} \bar{\xi}_r & \bar{\eta}_r \\ \bar{\xi}_z & \bar{\eta}_z \end{bmatrix} = \bar{\mathbf{J}}^{-1} = (\mathbf{J}|_{\xi=\eta=0})^{-1} \quad \text{and} \quad \bar{r} = r|_{\xi=\eta=0}. \tag{34}$$

The self-defined T-matrix is the transformation matrix between the vector of physical strain components and the vector of covariant strain components $\{\varepsilon_\xi, \varepsilon_\eta, \gamma_{\xi\eta}, \varepsilon_\theta\}^T$ evaluated at $\xi = \eta = 0$. Following the practice of Simo & Rifai [5], the expression for the physical strain in (33) is modified to be

$$\boldsymbol{\varepsilon}_\lambda = \frac{\bar{r}\det(\bar{\mathbf{J}})}{r\det(\mathbf{J})}\mathbf{T}\begin{bmatrix} \partial/\partial\xi & 0 \\ 0 & \partial/\partial\eta \\ \partial/\partial\eta & \partial/\partial\xi \\ \bar{\xi}_r/\bar{r} & \bar{\eta}_r/\bar{r} \end{bmatrix}\mathbf{M}\boldsymbol{\lambda} \tag{35}$$

with which (29) becomes

$$\int_{\Omega^e}\boldsymbol{\varepsilon}_\lambda d\Omega = 2\pi\int_{-1}^{+1}\int_{-1}^{+1}\boldsymbol{\varepsilon}_\lambda r\det(\mathbf{J})d\xi d\eta = 2\pi\bar{r}\det(\bar{\mathbf{J}})\mathbf{T}\int_{-1}^{+1}\int_{-1}^{+1}\begin{bmatrix} \partial/\partial\xi & 0 \\ 0 & \partial/\partial\eta \\ \partial/\partial\eta & \partial/\partial\xi \\ \bar{\xi}_r/\bar{r} & \bar{\eta}_r/\bar{r} \end{bmatrix}\mathbf{M}d\xi d\eta\cdot\boldsymbol{\lambda} = \mathbf{0} \tag{36}$$

or, simply,

$$\int_{-1}^{+1}\int_{-1}^{+1}\begin{bmatrix} \partial/\partial\xi & 0 \\ 0 & \partial/\partial\eta \\ \partial/\partial\eta & \partial/\partial\xi \\ \bar{\xi}_r/\bar{r} & \bar{\eta}_r/\bar{r} \end{bmatrix}\mathbf{M}d\xi d\eta = \mathbf{0} \tag{37}$$

Whilst the incompatible displacement shape function matrices of NQV and NCV families do not satisfy (37), the later can be fulfilled by simple modification of the shape functions.

5.2 Axisymmetric EAS-NQV Element

The incompatible modes of NQV have been introduced in Section 4.1. To fulfill (37), M_1 an M_2 are modified into

$$M_1 = (\frac{1}{3}-\xi^2)[1-\frac{\Delta_5}{2}(1-\eta)-\frac{\Delta_7}{2}(1+\eta)] \quad , \quad M_2 = (\frac{1}{3}-\eta^2)[1-\frac{\Delta_6}{2}(1+\xi)-\frac{\Delta_8}{2}(1-\xi)] \tag{38}$$

For the seven-node element, the modified bubble mode $(1/3\text{-}\xi^2)(1/3\text{-}\eta^2)$ in (25) and the non-vanished mode among (38) are both attempted. The predictions yielded by two version of seven-node are practically similar. For convenience, the above M_1 an M_2 are employed for the whole element family which is denoted as EAS-NQV.

5.3 Axisymmetric EAS-NCV Element

The incompatible modes of NQV have been introduced in Section 4.2. To fulfill (37), they are modified into

$$M_1 = (1/3 - \xi^2) - (N_5^* + N_7^*) \quad \text{and} \quad M_2 = (1/3 - \eta^2) - (N_6^* + N_8^*), \tag{39}$$

in which N_i^* is modified from N_i in (1) by replacing "1-|◇|" with "1/2-|◇|" for ◇ = ξ or η. This element family is denoted as EAS-NCV.

6. ERROR ESTIMATION AND STRESS RECOVERY

A key step in the adaptive analysis is the error estimation which identifies the parts of the mesh to be refined. Error is the difference between the exact value and the numerical solution. However, exact solution is not available for most engineering problems.

6.1 ZZ Error Estimator

Zienkiewicz and Zhu [24] brought forward the famous ZZ error estimator. The essence of the error estimator is to use a recovered solution constructed from the finite element prediction in place of the exact solution in computing the error [25]. To quantify the error, various norms can be used and the energy norm is a commonly accepted one. In the case of evaluating the stress error, the error in energy norm for a single element and the whole system can be respectively written as

$$\| \mathbf{e}_\sigma^* \|_e = \left[\int_{\Omega^e} (\boldsymbol{\sigma}^* - \boldsymbol{\sigma}_h)^T \mathbf{C}^{-1} (\boldsymbol{\sigma}^* - \boldsymbol{\sigma}_h) d\Omega \right]^{\frac{1}{2}} \quad \text{and} \quad \| \mathbf{e}_\sigma^* \| = \left[\sum^{NE} \left(\| \mathbf{e}_\sigma^* \|_e \right)^2 \right]^{\frac{1}{2}} \tag{40}$$

in which $\boldsymbol{\sigma}^*$ is the recovered stress, $\boldsymbol{\sigma}_h$ is the stress value directly obtained from FEM and *NE* is the total number of elements included in the whole system. Similarly, the estimated energy norm for an element and the system are respectively:

$$\| \mathbf{u}_\sigma^* \|_e = \left[\int_{\Omega^e} \boldsymbol{\sigma}_h^T \mathbf{C}^{-1} \boldsymbol{\sigma}_h d\Omega \right]^{\frac{1}{2}} \quad \text{and} \quad \| \mathbf{u}_\sigma^* \| = \left[\sum^{NE} \left(\| \mathbf{u}_\sigma^* \|_e \right)^2 \right]^{\frac{1}{2}} \tag{41}$$

The estimated energy norm of the exact solution is often approximated as:

$$\| \bar{\mathbf{u}} \| = \left[\| \mathbf{u}_\sigma^* \|^2 + \| \mathbf{e}_\sigma^* \|^2 \right]^{\frac{1}{2}}. \tag{42}$$

The estimated relative error is computed as

$$\eta^* = (\| \mathbf{e}_\sigma^* \| / \| \bar{\mathbf{u}} \|) \times 100\% \tag{43}$$

Zienkiewicz & Zhu [24] have proven that if the recovered stress is asymptotically exact, the above estimated error always converges to the exact one when the mesh is continuously refined. The adaptive analysis cycle stops when the estimated relative error is smaller than a prescribed target value η_t. For an individual element, the estimated relative error can be expressed as

$$\eta_i^* = \sqrt{\frac{\| \mathbf{e}_\sigma^* \|_e^2}{\| \bar{\mathbf{u}} \|^2 / NE}} \times 100\% , \tag{44}$$

and the element will be refined if $\eta_i^* > \eta_t$.

6.2 Stress Recovery

When Zienkiewicz and Zhu first brought forward their error estimator, recovery methods including simple nodal average, L_2 projection and global stress smooth were used to obtain the recovered values. Later, Zienkiewicz and Zhu [26-27] introduced the superconvergent patch recovery (SPR) technique. The simplicity and the effectiveness of the recovery technique enable the wide application of ZZ error estimator.

In SPR, a patch composed of elements sharing a common non-boundary node which is termed as assembly node is formed first as shown in Figure 3. The stress distribution within the patch is least square fitted by a polynomial which is of the same order as the displacement interpolation of a regular element. With the four-node element as the regular element, each of the stress component σ^* is taken to be

$$\sigma^* = \mathbf{Qa} = [1,\ r - r_0,\ z - z_0,\ (r - r_0)(z - z_0)]\{ a_1 \quad \cdots \quad a_4 \}^T \tag{45}$$

where **a** is the vector of coefficients to be determined and (r_0, z_0) is the coordinate of the assembly node. By minimizing

$$S(\mathbf{a}) = \sum_{i=1}^{n} \left(\sigma_h(r_i, z_i) - \sigma^*(r_i, z_i) \right)^2 = \sum_{i=1}^{n} \left(\sigma_h(r_i, z_i) - \mathbf{Q}(r_i, z_i)\mathbf{a} \right)^2 \tag{46}$$

with respect to **a**,

$$\mathbf{a} = [\sum_{j=1}^{n} \mathbf{Q}^T(r_j, z_j)\mathbf{Q}(r_j, z_j)]^{-1}[\sum_{i=1}^{n} \mathbf{Q}(r_i, z_i)^T \sigma_h(r_i, z_i)]\,. \tag{47}$$

In the equations, n denotes the number of stress sampling points and σ_h denotes the direct unprocessed finite element stress solution. The least-square fitted stresses at the assembly node can be obtained with the solved values of **a** and (45). Detailed implementation of SPR technique can be found in Ref. [13, 26-27].

7. NUMERICAL EXAMPLES

To study the performance of the new transition element families developed in this paper, several numerical examples will be conducted. The error in energy norm yielded by different transition element families in adaptive analyses will be compared. In all analyses, the same regular four-node element will adopt the following EAS field:

$$\boldsymbol{\varepsilon}_\lambda = \frac{\bar{r}\det(\bar{\mathbf{J}})}{r\det(\mathbf{J})}\mathbf{T}\begin{bmatrix} \partial/\partial\xi & 0 \\ 0 & \partial/\partial\eta \\ \partial/\partial\eta & \partial/\partial\xi \\ \bar{\xi}_r/\bar{r} & \bar{\eta}_r/\bar{r} \end{bmatrix}\begin{bmatrix} 1/3-\xi^2 & 0 & 1/3-\eta^2 & 0 \\ 0 & 1/3-\xi^2 & 0 & 1/3-\eta^2 \end{bmatrix}\boldsymbol{\lambda}$$

which employs the modified incompatible modes of Wilson et al [28].

Abbreviations of the transitional element families to be compared in this section are summarized below:

- FI : the fully integrated (with the 2nd order quadrature) compatible displacement elements, see section 2.
- AHS-10 and AHS-12: The newly developed hybrid-stress transition element families with 10 and 12 equilibrating stress modes, see (18) and (19), respectively.
- NQV: the incompatible transition element family of Choi et al [12], see Section 4.1.
- NCV: the incompatible transition element family using the incompatible modes degenerated from 3D family of Choi and Lee [15], see Section 4.2.
- EAS-NQV: the EAS counterpart of NQV devised in this paper, see Section 5.2.

- EAS-NCV: the EAS counterpart of NCV devised in this paper, see Section 5.3.

For all newly developed elements, a thick-walled cylinder modeled by five quadrilateral elements as shown in Figure 4 is considered. Mid-side nodes are randomly added to element edges to form transition elements in the mesh. On all geometry boundaries, $u_r = 2r$ and $u_z = 1+4z$ are prescribed [3]. Exact displacements and stress are reproduced by all element families. In other words, all the element families pass the patch test.

In the following sub-sections, five problems are analyzed by the transition element families. In each example, meshes will be generated and the total errors in the regular and transition elements will be compared. To keep this paper short, only the meshes generated by AHS-10 will be shown. As the number of transition elements is typically below 10% of the element population, the total error is dominated by the regular elements. To better illustrate the relative accuracy of different transition element families, the meshes generated by NQV are used by all families and the error sums in the transition elements, i.e.

$$\| \mathbf{e}_{\text{Tran.Err.}} \| = \left[\sum_{i=1}^{m} (\| \mathbf{e}_{\sigma} \|_e)^2 \right]^{\frac{1}{2}} \tag{48}$$

where m refers to the number of transition elements in the mesh, are computed. As usual, exact and estimated errors are adopted for problems with and without analytical solutions, respectively. These errors are plotted against nDOF which denotes the total number of degree of freedom for the whole system. In case that the first and/or the second adaptive meshes do not contain any transition elements, the value of $\|\mathbf{e}_{\text{Tran.Err.}}\|$ is zero and will not be presented in the comparison of errors in transition elements. It should also be noted that $\|\mathbf{e}_{\text{Tran.Err.}}\|$ can go up as the percentage of the total volume of the transition elements goes up. As a result, while the log-log plots for $\|\mathbf{e}\|$ versus nDOF are essentially straight lines, the ones for $\|\mathbf{e}_{\text{Tran.Err.}}\|$ versus nDOF often exhibit “kinks” in the figures. In all examples, EAS-NQV and EAS-NCV always show similar accuracy as NQV and NCV respectively. For graphical clarity, results of EAS-NQV and NQV will be displayed by a single line and the same practice applies to EAS-NCV and NCV.

7. 1 Thick Hollow Sphere

A thick hollow sphere with outer radius R_o = 20 and inner radius R_i = 5 subjected to internal pressure P is studied. Owing to symmetry, only half of the sphere in the r-z-plane is modeled as shown in Figure 5(a). The analytical strains are [29]:

$$\varepsilon_r = (aR^5 - 2bR^2 + 3z^2b) / R^5 \quad , \quad \varepsilon_z = (-3z^2b + aR^5 + bR^2) / R^5 \quad ,$$

$$\gamma_{rz} = -3(r^2b + 3aR^5 - 3aR^3z^2 + 4bR^2 - 4z^2b)z / (R^5r) \quad , \quad \varepsilon_\theta = (aR^3 + b) / R^3 \tag{49}$$

in which

$$a = \frac{PR_i^3}{(3\lambda + 2\mu)(R_o^3 - R_i^3)}, \quad b = \frac{PR_i^3R_o^3}{4\mu(R_o^3 - R_i^3)} \quad \text{and} \quad R^2 = r^2 + z^2 . \tag{50}$$

Moreover, λ and μ are Lame's constants. Exact stresses can be obtained through (4). In this problem, the exact error is evaluated. The target relative error η_t is set at 3% which is attained in six adaptive steps, see Figure 5(b) for the corresponding meshes. Comparison of the total errors when different transition element families are employed can be seen in Figure 5(c) whilst comparison of the errors in transition elements is given in Figure 5(d).

7. 2 Cylinder with a Spherical Hole

This problem considers a ϕ20 cylinder with a central ϕ2 spherical cavity subjected to a uniform axial tension. Owing to symmetry, only half of the cylinder in the r-z-plane is modeled as shown in Figure 6(a). The target relative error η_t is set at 0.5% which is achieved in six adaptive steps. Pertinent adaptive meshes are given in Figure 6(b). Comparison of the total errors when different transition element families are employed is provided in Figure 6(c). On the other hand, comparison of the errors in transition elements can be noted in Figure 6(d).

7. 3 Cylinder with a Penny Crack

A ϕ4 cylinder with a ϕ2 penny crack located at its centre subjected to a uniform tension along *z*-axis is studied. Owing to symmetry, only half of the problem domain in the r-z-plane is modeled as shown in Figure 7(a). The target relative error η_t is set at 4%. As a result of the stress

singularity, dense meshes form around the crack-tip as shown in Figure 7(b). Eight adaptive steps are required to attain the specified η_t. Comparison of the total errors when different transition element families are employed is given in Figure 7(c). Figure 7(d) shows the errors in the transition elements.

7. 4 Cylinder-Shaped Vessel

This problem studies a ϕ4 cylinder-shaped vessel with a ϕ2 cylindrical cavity subjected to a uniform axial tension as depicted in Figure 8(a). According to symmetry, only half of the vessel is modeled. The target relative error is set at 2% which is attained in seven steps, see Figure 8(b) for pertinent meshes. Comparison of the total errors when different transition element families are adopted can be seen in Figure 8(c). On the other hand, comparison of the errors in transition elements is given in Figure 8(d).

7. 5 Machine Part

In this example, an axisymmetric machine part subjected to uniform tensile loading is studied as depicted in Figure 9(a). The target relative error is set at 2% which is achieved in four steps, see Figure 9(b) for adaptive meshes. One can obviously find more nodes and elements located around the areas where stress concentrations are expected. Comparisons of total errors between different transition element families can be found in Figure 9(c). And, comparisons of errors in transition elements can be found in Figure 9(d).

7. 6 Discussion for Adaptive Analyses

From the five examples, one can noted that the two newly developed hybrid-stress transition element families AHS-10 and AHS-12 deliver the highest accuracy. Among them, the former is not only marginally more accurate but also more efficient. For the EAS and incompatible element families, the accuracy of the EAS families is close to that of the respective incompatible families. However, the efficiency of the EAS elements surpasses that of the incompatible elements which, for the patch test fulfillment, requires a computed correction to the incompatible B-matrices. In most examples, NCV and EAS-NCV are slightly more accurate than NQV and EAS-NQV.

8. CONCLUSION

In this paper, existing displacement compatible and incompatible transition elements for adaptive analyses of axisymmetric elastic problems are briefly reviewed. Two hybrid-stress and two EAS transition element families are developed. Numerical examples are presented to compare the accuracy of various transition element families.

For the hybrid-stress transition element, the five-node elements are noted to be dominating in number among the five- to seven-node transition elements. In this light, a complete linear field in r and z for ($r\sigma_r$, σ_θ, $r\sigma_z$, $r\tau_{rz}$) possessing ten modes which can marginally secure the proper rank of the five-node element are identified. Following our practice in plane and 3D problems, the stress field is employed by all members of the transition element family which is termed AHS-10. To study the effect of including additional stress modes, another less efficient family termed AHS-12 with two extra stress modes is also implied. From the numerical results, AHS-10 marginally surpasses AHS-12 in accuracy.

The EAS transition element families are based on NQV and NCV incompatible element families of Choi et al [12, 15]. Through modifying the strain and the incompatible displacement defined with respect to the natural coordinates of the element, transition element families EAS-NQV and EAS-NCV are derived. Unlike the incompatible elements, the computational correction on incompatible B-matrix for the patch test fulfillment is exempted. On the other hand, the EAS families produce graphically undistinguishable accuracy with respect to the pertinent incompatible ones.

Among the four new families, AHS-10 delivers the highest accuracy which is marginally better than that of AHS-12. The EAS/incompatible families are more accurate than the fully integrated compatible displacement element family but less accurate than the hybrid-stress families. Among the EAS/incompatible families, EAS-NCV/NCV are slightly more accurate than EAS-NQV/NQV in accuracy.

REFERENCE

1. Li LY & Bettess P. Adaptive finite element methods: A review. *Applied Mechanics Reviews* **50**, 581-591 (1997).
2. Bachrach WE & Belytschko T. Axisymmetric elements with high coarse-mesh accuracy *Computers and Structures* **23**, 323-331 (1986).
3. Chen WJ & Cheung YK. Nonconforming element method and refined hybrid element method for axisymmetric solid. *International Journal for Numerical Methods in Engineering* **39**, 2509-2529 (1996).
4. Kasper EP & Taylor RL. Mixed-enhanced formulation for geometrically linear axisymmetric problems. *International Journal for Numerical Methods in Engineering* **53**, 2061-2086 (2002).
5. Simo JC & Rifai MS. Class of mixed assumed strain methods and the method of incompatible modes. *International Journal for Numerical Methods in Engineering* **29**, 1595-1638 (1990).
6. Spilker RL. Improved hybrid-stress axisymmetric elements includng behaviour for nearly incompressible materials. *International Journal for Numerical Methods in Engineering* **17**, 483-501 (1981).
7. Sze KY & Chow CL. Incompatible element for axisymmetric structure and its modification by hybrid method. *International Journal for Numerical Methods in Engineering* **31**, 385-405 (1991).
8. Tian ZS & Pian HH. Axisymmetric solid elements by a rational hybrid stress method. *Computers and Structures* **20**, 141-149 (1984).
9. Weissman SL & Taylor RL. Four-node axisymmetric element based upon the Hellinger-Reissner functional. *Computer Methods in Applied Mechanics and Engineering* **85**, 39-55 (1991).
10. Wu CC & Cheung YK. The patch test condition in curvilinear coordinates - formulation and application. *Science in China,Ser.A* **8**, 849-858 (1992).
11. Zhou XX, Chow YK & Leung CF. Application of enhanced assumed strain finite element method to predict collapse loads of undrained geotechnical problems. *International Journal for Numerical and Analytical Methods in Geomechanics* **31**, 1033-1043 (2007).
12. Choi CK & Lee EJ. Nonconforming variable-node axisymmetric solid element. *Journal of Engineering Mechanics* **130**, 578-588 (2004).
13. Wu D, Sze KY & Lo SH. Two- and three-dimensional transition elements for adaptive refinement analysis of elasticity problems. *International Journal for Numerical Methods in Engineering* **78**, 587-630 (2008).
14. Lo SH, Wu D & Sze KY. Adaptive meshing and analysis using transitional quadrilateral and hexahedral elements. *Finite Elements in Analysis and Design* **46**, 2-16 (2010).
15. Choi CK & Lee NH. Three dimensional transition solid elements for adaptive mesh gradation. *Structural Engineering and Mechanics* **1**, 61-74 (1993).
16. Wan KH, Transition finite elements for mesh refinement in plane and plate bending analysis, M.Phil. Thesis, Mechanical Engineering, The University of Hong Kong (2004)
17. Lo SH, Wan KH & Sze KY. Adaptive refinement analysis using hybrid-stress transition elements. *Computers and Structures* **84**, 2212-2230 (2006).

18. Gupta AK. A finite element for transition from a fine to a coarse grid. *International Journal for Numerical Methods in Engineering* **12**, 35-45 (1978).
19. Pian THH & Sumihara K. Rational approach for assumed stress finite elements. *International Journal for Numerical Methods in Engineering* **20**, 1685-1695 (1984).
20. Pian THH & Tong P. Relations between incompatible displacement model and hybrid stress model. *International Journal for Numerical Methods in Engineering* **22**, 173-181 (1986).
21. Jog CS & Annabattula R. The development of hybrid axisymmetric elements based on the Hellinger-Reissner variational principle. *International Journal for Numerical Methods in Engineering* **65**, 2279-2291 (2006).
22. Spliker RL & Pian THH. A study of axisymmetric solid of revolution elements based on assumed stress hybrid model *Computers & Structures* **9**, 273-279 (1978).
23. Taylor RL, Beresford PJ & Wilson EL. A non-conforming element for stress analysis. *International Journal for Numerical Methods in Engineering* **10**, 1211-1219 (1976).
24. Zienkiewicz OC & Zhu JZ. A simple error estimator and adaptive procedure for practical engineering analysis. *International Journal for Numerical Methods in Engineering* **24**, 337-357 (1987).
25. Zhu JZ & Zienkiewicz OC. A posteriori error estimation and three-dimensional automatic mesh generation. *Finite Elements in Analysis and Design* **25**, 167-184 (1997).
26. Zienkiewicz OC & Zhu JZ. Superconvergent patch recovery and a posteriori error estimates. Part 1: the recovery technique. *International Journal for Numerical Methods in Engineering* **33**, 1331-1364 (1992).
27. Zienkiewicz OC & Zhu JZ. Superconvergent patch recovery and a posteriori error estimates. Part 2: error estimates and adaptivity. *International Journal for Numerical Methods in Engineering* **33**, 1365-1382 (1992).
28. Wilson EL, Taylor RL, Doherty WD & Ghaboussi J. Incompatible displacement models (Academic Press, New York, 1973).
29. Atanackovic TM & Guran A. Theory of elasticity for scientists and engineers (Birkhauser, Boston, 2000).

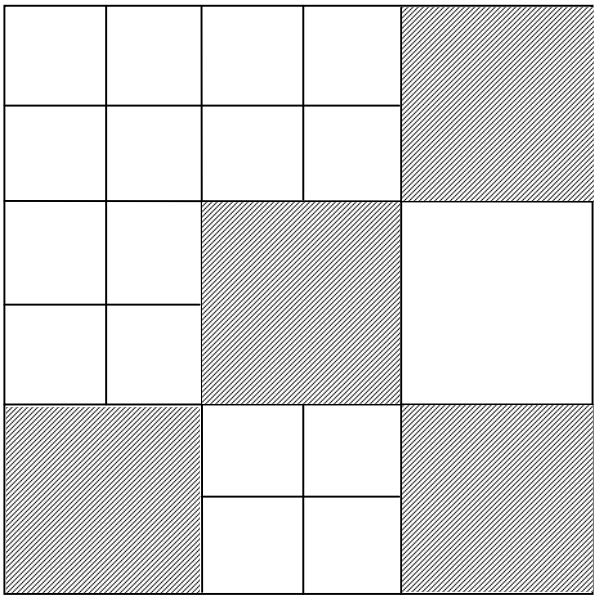

Figure 1. A mesh containing the regular (blank) and transition (hatched) elements.

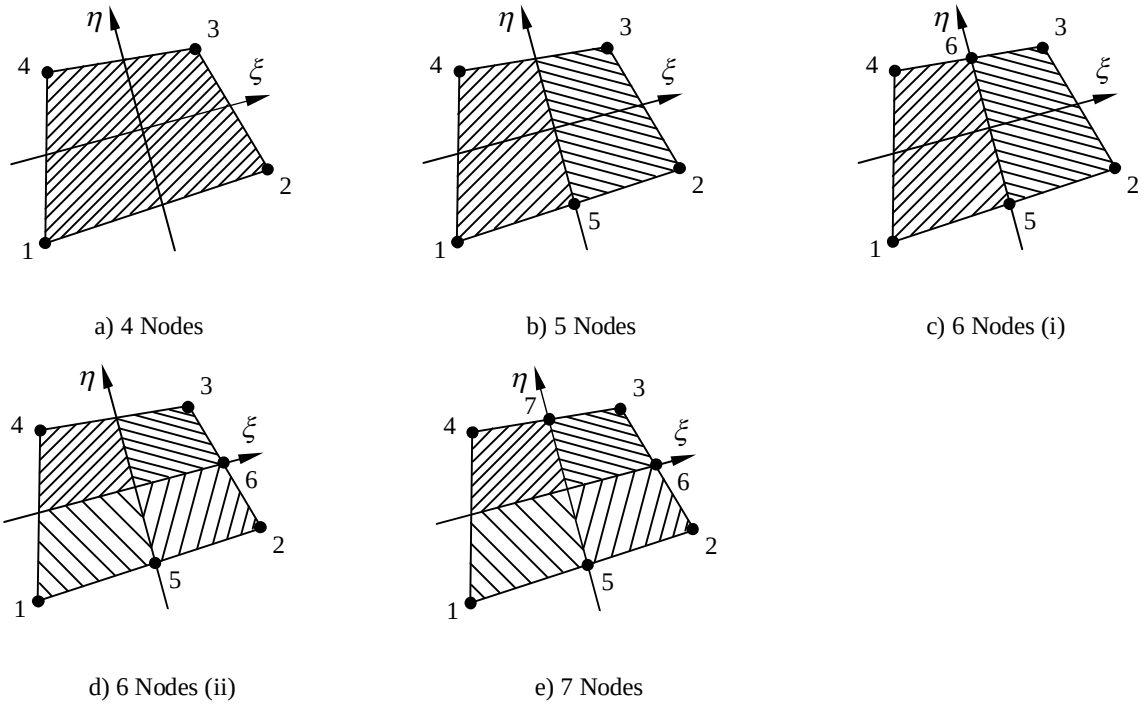

a) 4 Nodes

b) 5 Nodes

c) 6 Nodes (i)

d) 6 Nodes (ii)

e) 7 Nodes

Figure 2. (a) Regular element and (b)-(e) transition elements with different mid-side nodes. If exists, node 8 bisects nodes 1 and 4. Different integration zones are hatched differently.

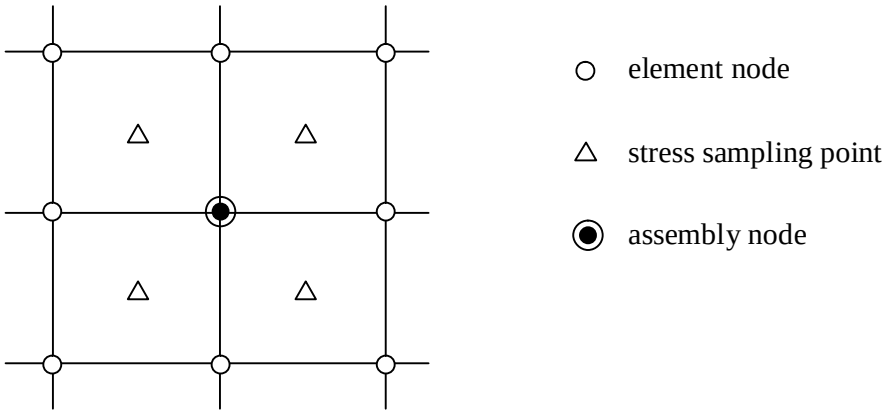

Figure 3. A patch for superconvergent patch recovery.

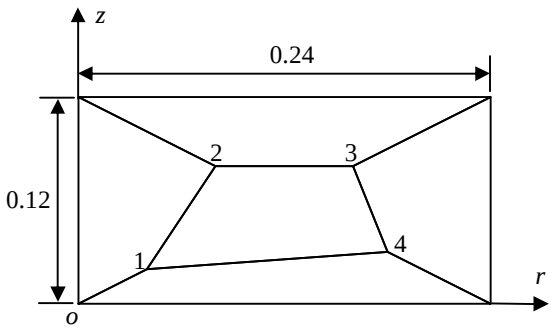

Coordinates of inner nodes

Node	*r*	*z*
1	0.04	0.02
2	0.08	0.08
3	0.16	0.08
4	0.18	0.03

Figure 4. Mesh for patch test.

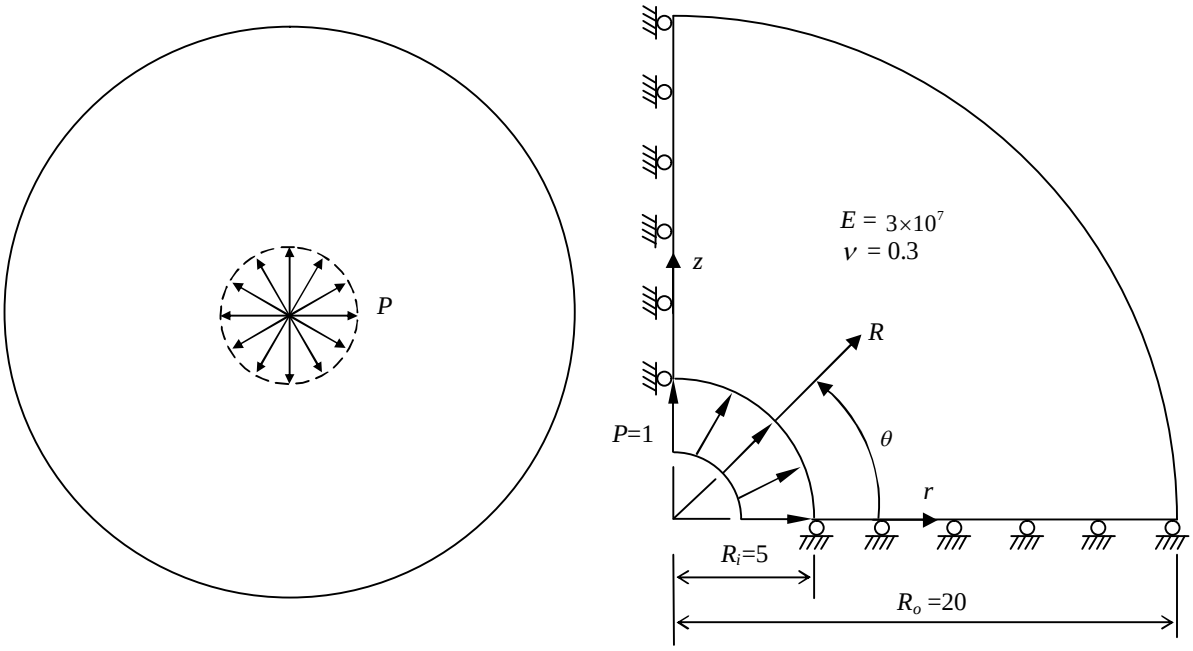

(a)

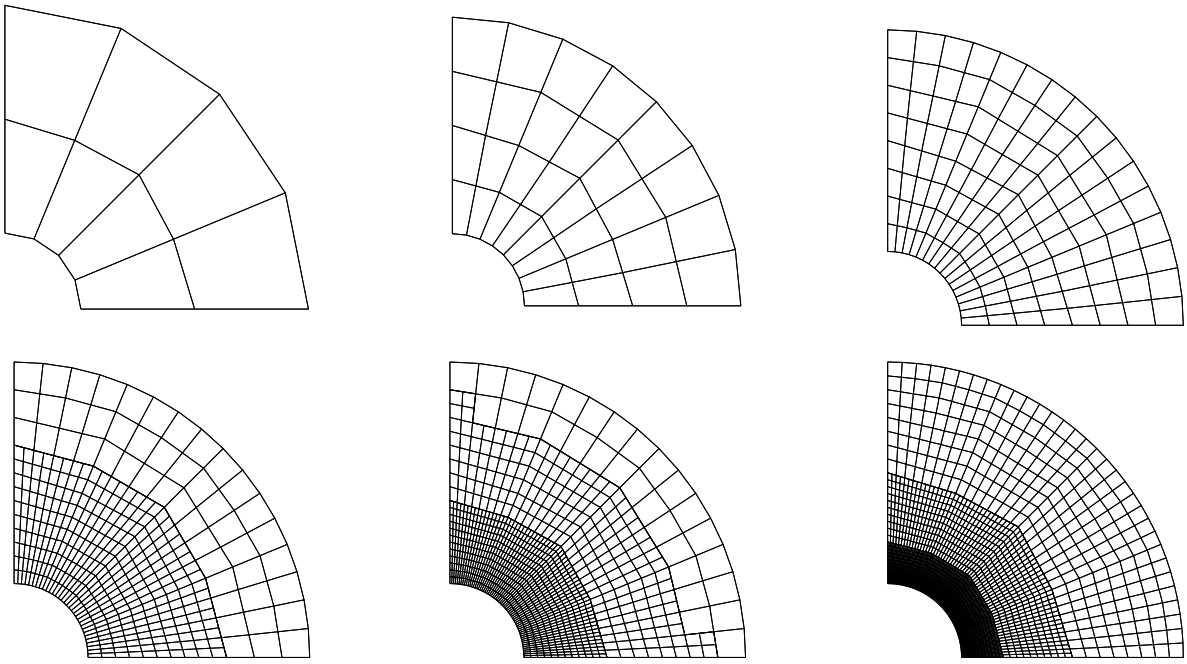

(b)

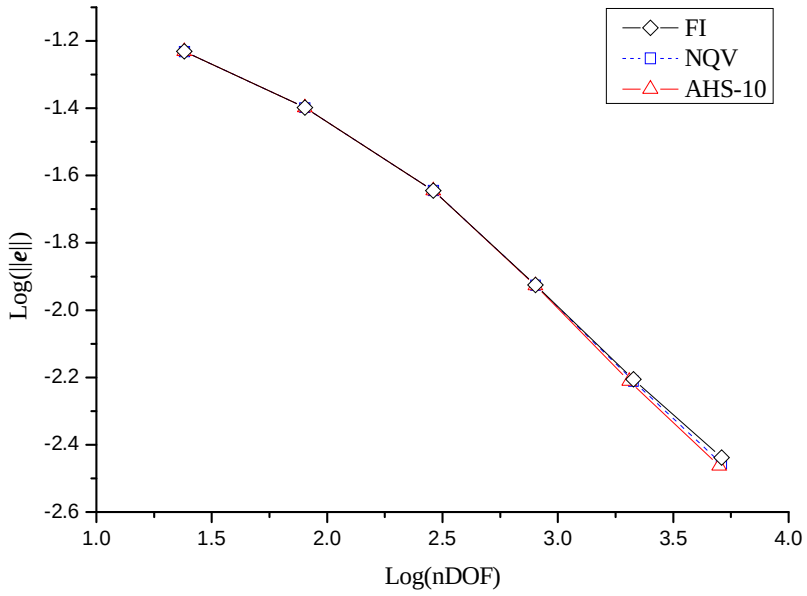

(c)

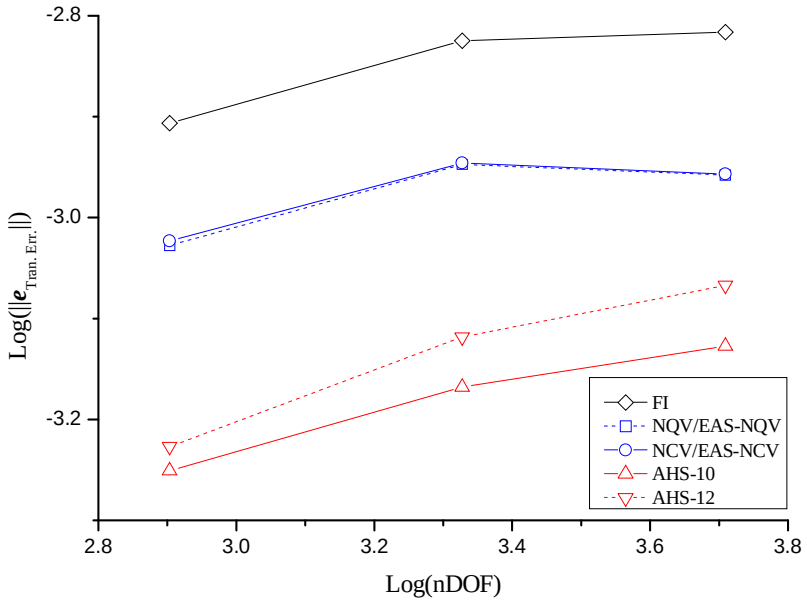

(d)

Figure 5. Thick hollow sphere. (a) Problem specification, (b) meshes, (c) total errors comparison, (d) comparison of errors in transition elements.

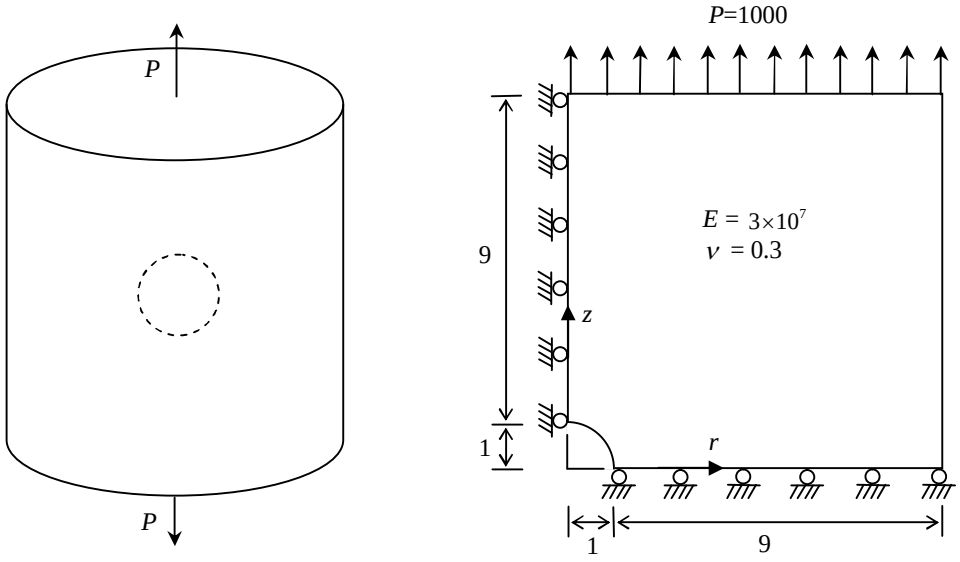

(a)

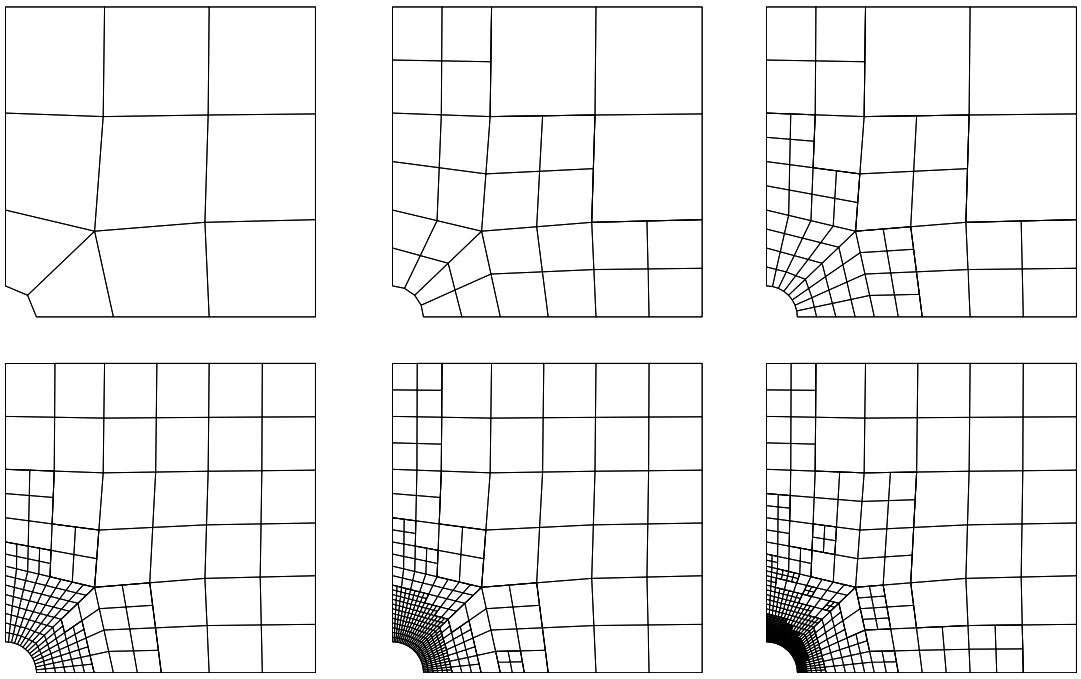

(b)

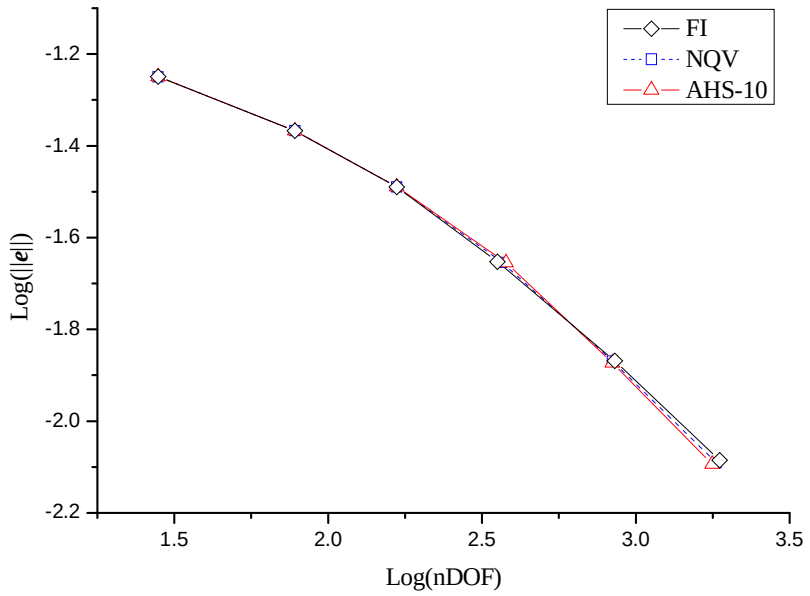

(c)

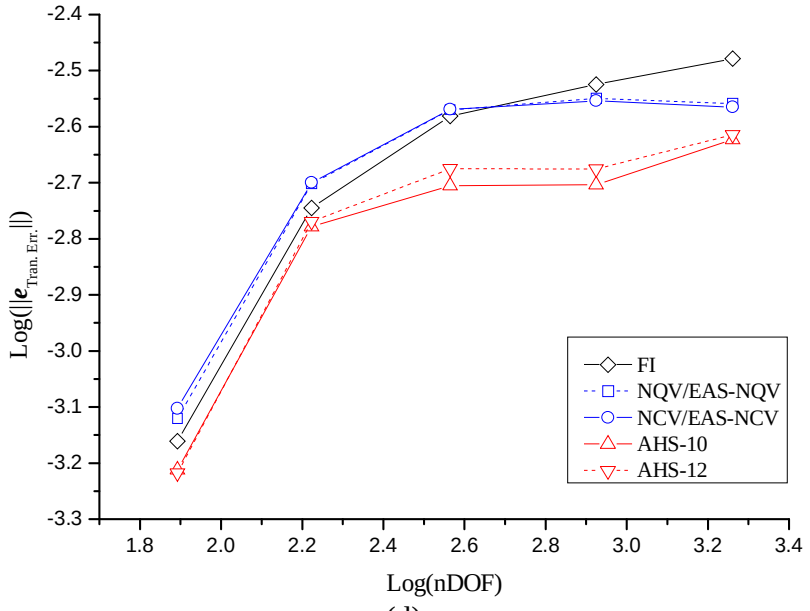

(d)

Figure 6. Cylinder with a spherical hole problem. (a) Problem specification, (b) meshes, (c) total errors comparison, (d) comparison of errors in transition elements.

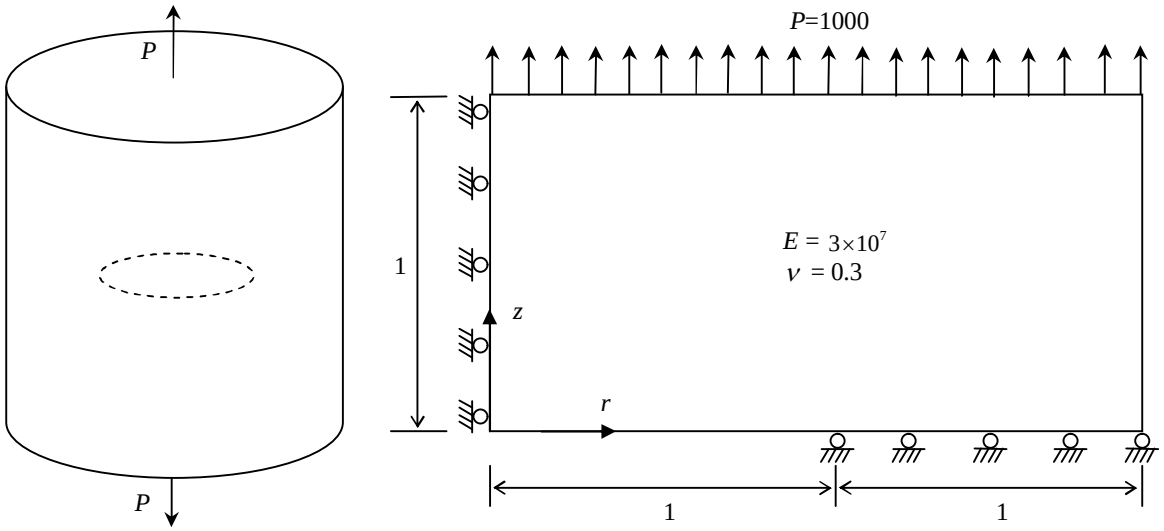

(a)

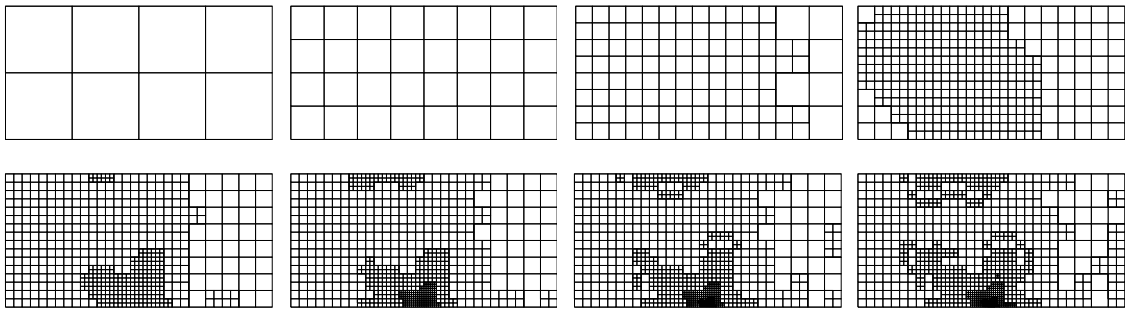

(b)

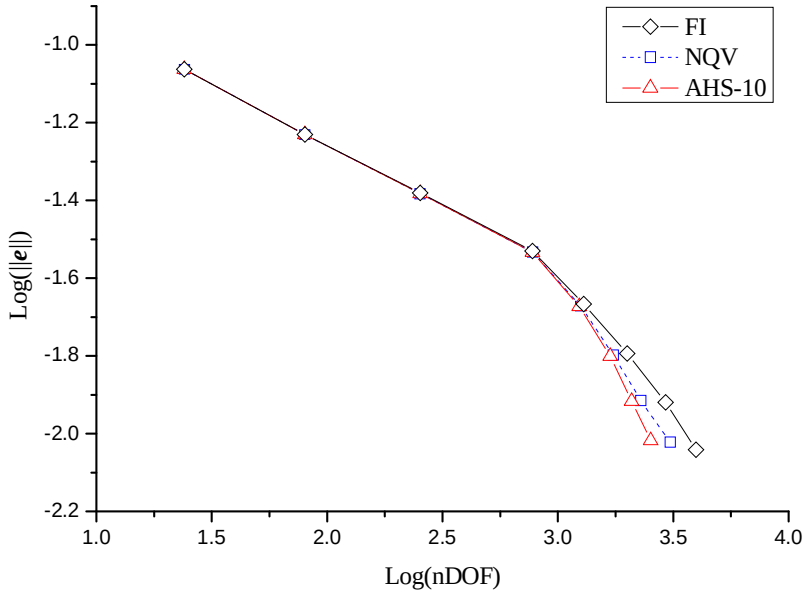

(c)

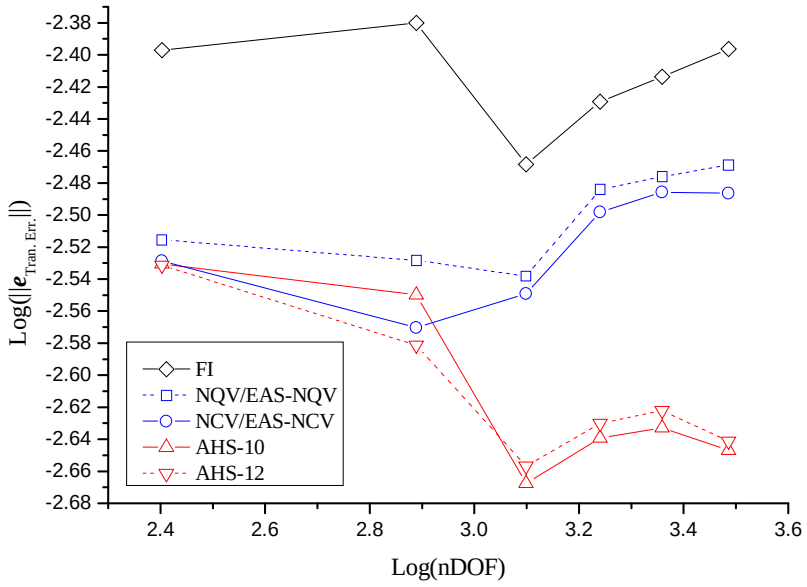

(d)

Figure 7. Cylinder with a penny crack problem. (a) Problem specification, (b) meshes, (c) total errors comparison, (d) comparison of errors in transition elements.

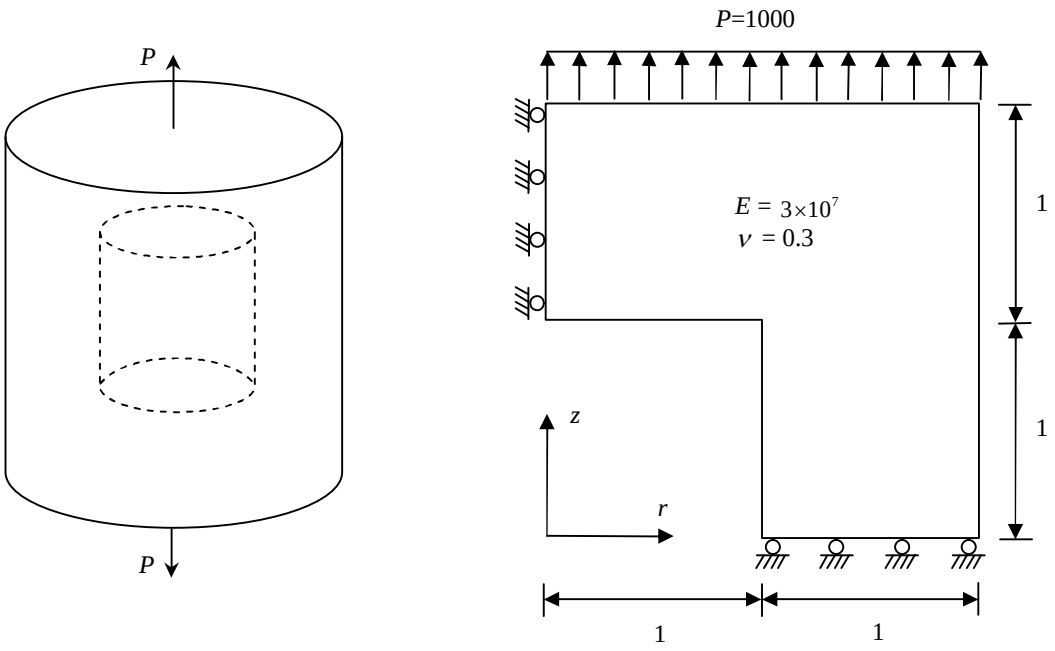

(a)

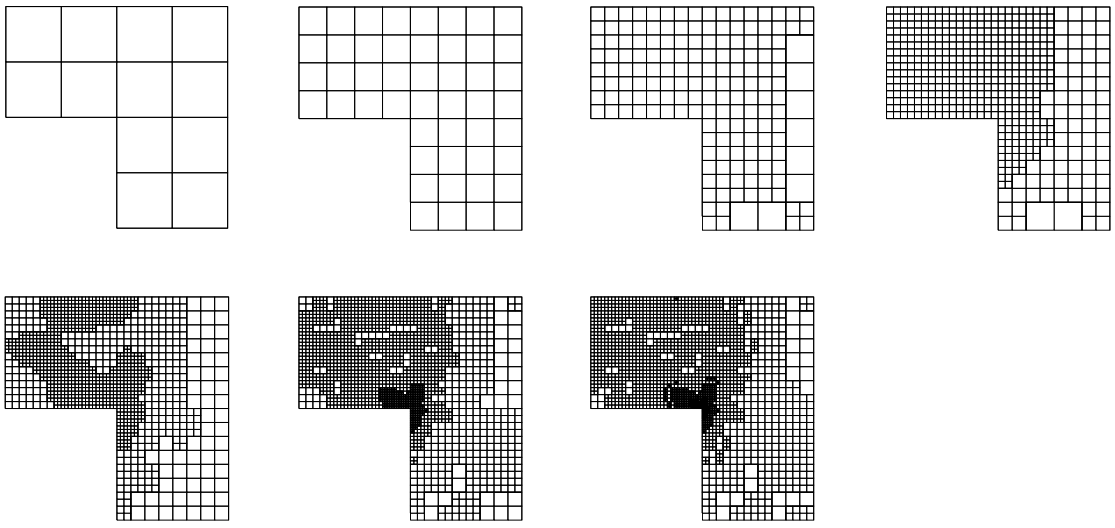

(b)

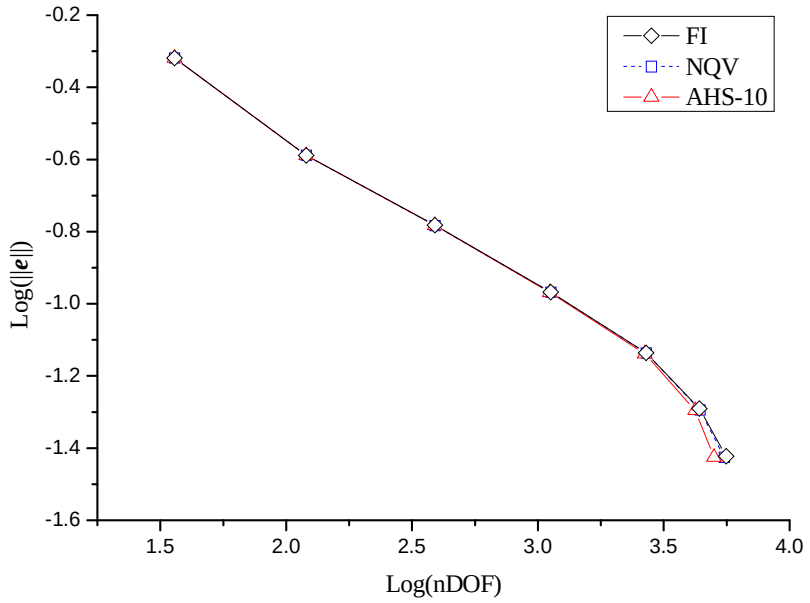

(c)

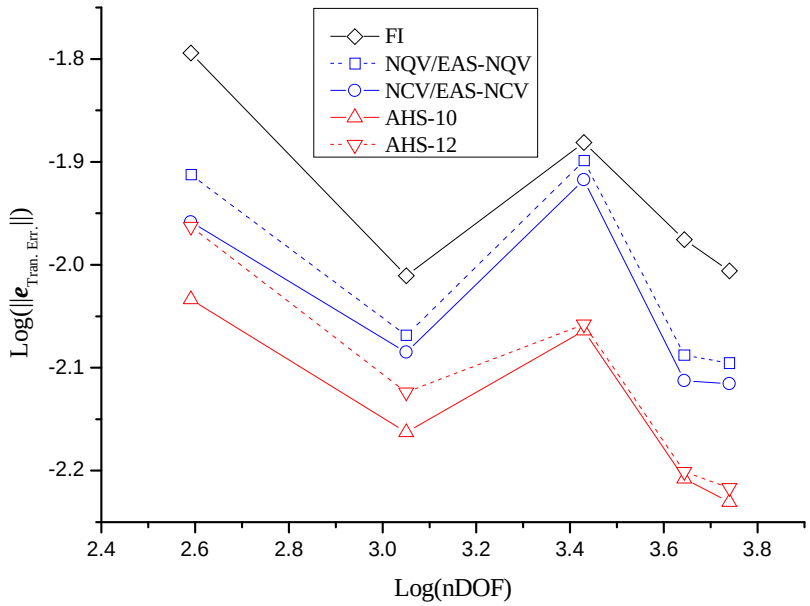

(d)

Figure 8. The cylinder-shaped vessel problem. (a) Problem specification, (b) meshes, (c) total errors comparison, (d) comparison of errors in transition elements.

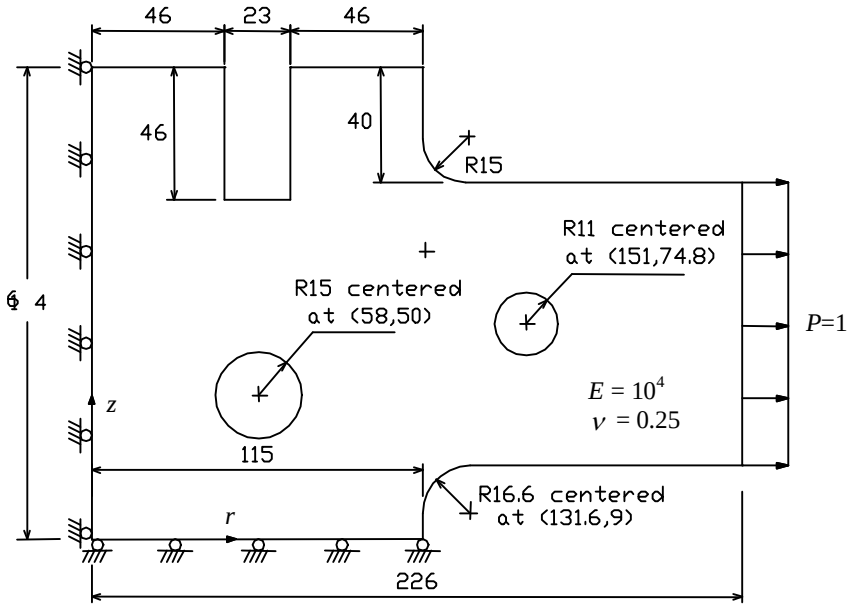
46
23
46
46
40
R15
R11 centered
at (151,74.8)
R15 centered
at (58,50)
P=1
E = 10^4
ν = 0.25
z
r
115
R16.6 centered
at (131.6,9)
226

(a)

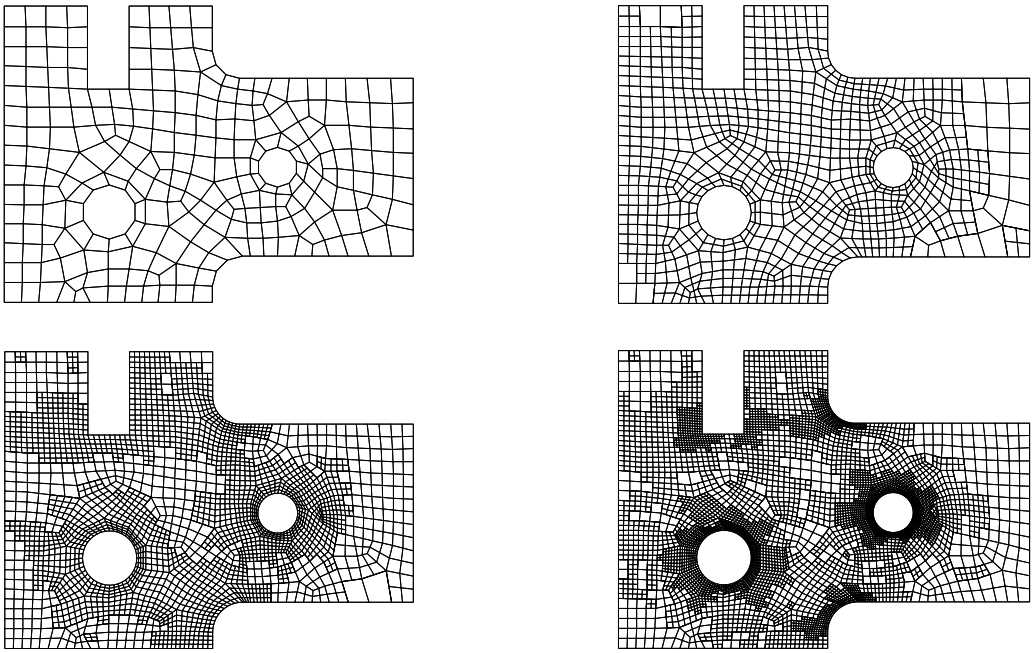

(b)

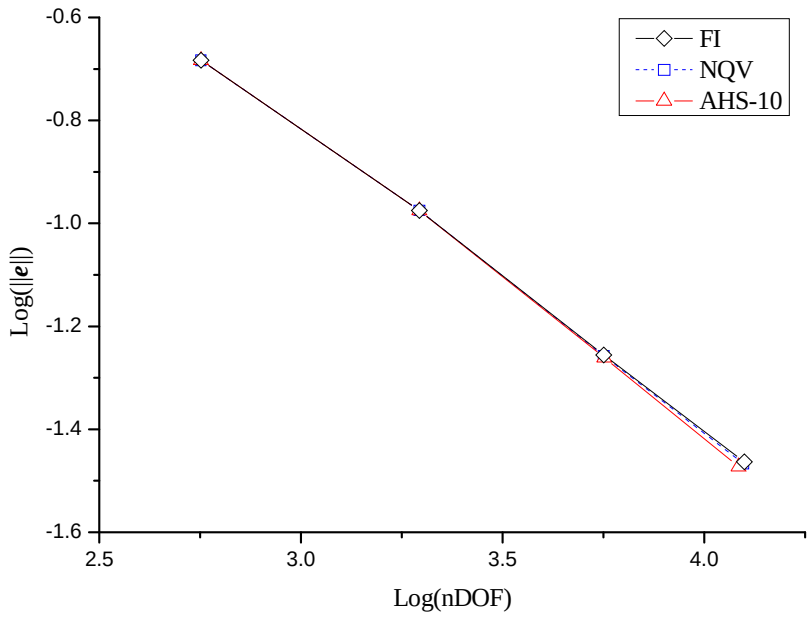

(c)

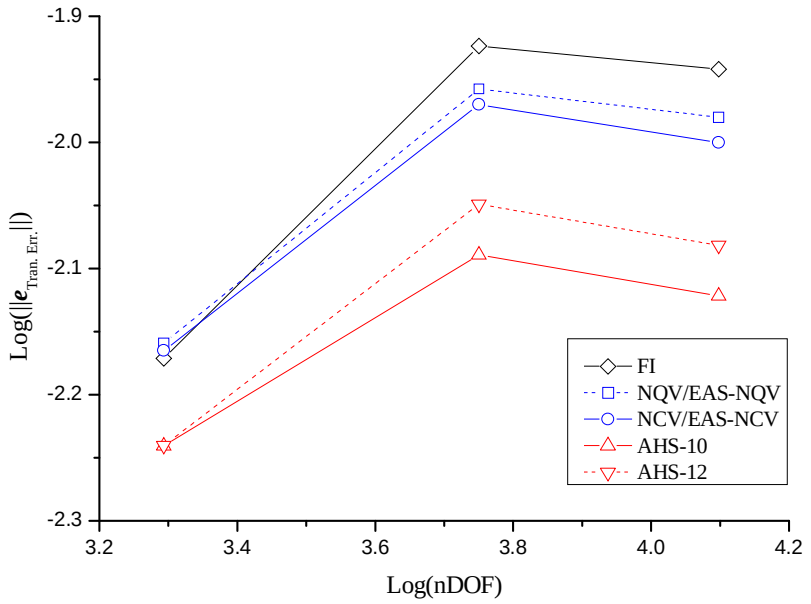

(d)

Figure 9. The machine part problem. (a) Problem specification, (b) meshes, (c) total errors comparison, (d) comparison of errors in transition elements.